UC Irvine
UC Irvine Previously Published Works

Title

Hippocampal dentate gyrus integrity revealed with ultrahigh resolution diffusion imaging predicts memory performance in older adults.

Permalink

https://escholarship.org/uc/item/6np1g60g

Journal

Hippocampus, 32(9)

ISSN

1050-9631

Authors

Granger, Steven J
Colon-Perez, Luis
Larson, Myra Saraí
et al.

Publication Date

2022-09-01

DOI

10.1002/hipo.23456

Copyright Information

Peer reviewed

RESEARCH ARTICLE

WILEY

Hippocampal dentate gyrus integrity revealed with ultrahigh resolution diffusion imaging predicts memory performance in older adults

Steven J. Granger[1,2] | Luis Colon-Perez[1,2] | Myra Saraí Larson[1,2] |
Michael Phelan[3] | David B. Keator[4] | John T. Janecek[1,2] |
Mithra T. Sathishkumar[1,2] | Anna P. Smith[1,2] | Liv McMillan[1,2] | Dana Greenia[5] |
Maria M. Corrada[5] | Claudia H. Kawas[1,2,5] | Michael A. Yassa[1,2,4,5]

[1]Center for the Neurobiology of Learning and Memory, University of California, Irvine, California, USA

[2]Department of Neurobiology and Behavior, University of California, Irvine, California, USA

[3]UC Institute for Memory Impairments and Neurological Disorders, University of California, Irvine, California, USA

[4]Department of Psychiatry and Human Behavior, University of California, Irvine, California, USA

[5]Department of Neurology, University of California, Irvine, California, USA

Correspondence
Michael A. Yassa, University of California, 1418 Biological Sciences III, Irvine, CA 92697-4550, USA.
Email: michael.yassa@uci.edu

Abstract

Medial temporal lobe (MTL) atrophy is a core feature of age-related cognitive decline and Alzheimer's disease (AD). While regional volumes and thickness are often used as a proxy for neurodegeneration, they lack the sensitivity to serve as an accurate diagnostic test and indicate advanced neurodegeneration. Here, we used a submillimeter resolution diffusion weighted MRI sequence (ZOOMit) to quantify microstructural properties of hippocampal subfields in older adults (63–98 years old) using tensor derived measures: fractional anisotropy (FA) and mean diffusivity (MD). We demonstrate that the high-resolution sequence, and not a standard resolution sequence, identifies dissociable profiles for CA1, dentate gyrus (DG), and the collateral sulcus. Using ZOOMit, we show that advanced age is associated with increased MD of the CA1 and DG as well as decreased FA of the DG. Increased MD of the DG, reflecting decreased cellular density, mediated the relationship between age and word list recall. Further, increased MD in the DG, but not DG volume, was linked to worse spatial pattern separation. Our results demonstrate that ultrahigh-resolution diffusion imaging enables the detection of microstructural differences in hippocampal subfield integrity and will lead to novel insights into the mechanisms of age-related memory loss.

KEYWORDS
aging, dentate gyrus, hippocampus, magnetic resonance imaging, memory

1 | INTRODUCTION

Episodic memory decline and medial temporal lobe (MTL) atrophy are prominent changes associated with age-related cognitive decline (Braak & Braak, 1991; Gomez-Isla et al., 1996; Jack et al., 1999; Price et al., 2001). Early sites of structural atrophy include the hippocampus (Fox & Freeborough, 1997; Sabuncu et al., 2011), including specific subfields such as the dentate gyrus (DG; Ohm, 2007; Yassa

et al., 2011, Dillon et al., 2017) and CA1 (Csernansky et al., 2000; Csernansky et al., 2005), as well as the adjacent entorhinal cortex (Gomez-Isla et al., 1996). On a cellular level, structural alterations including reduced neuron count and reduced dendritic arborization are a core biological phenomenon associated with age-related cognitive decline that signal tissue destabilization (Ohm, 2007; Zarow et al., 2005). In humans, changes in regional volumes and thickness are most commonly used as a proxy for large scale structural atrophy

and neurodegeneration (Márquez & Yassa, 2019), however, they do not provide any insights regarding microstructural MTL neurodegeneration hallmarks like cellular loss nor dendritic arborization. It has been suggested that the study of volumes lack the specificity to stand alone as an accurate diagnostic test to distinguish normal aging from Alzheimer's disease (AD) and usually indicate an advanced stage of neurodegeneration providing little room for targeted interventional therapy (Teipel et al., 2013; Frisoni et al., 2010; Whittaker et al., 2018). Therefore, there is substantial need for sensitive and specific markers of microstructural atrophy due to aging and aging-related pathologies. These potential new biomarkers should provide improved quantification of the microstructural changes that underlie gross volumetric decline and provide insight into cellular atrophy in humans.

Measures derived from diffusion weighted MRI (dMRI) are emerging as strong candidates for novel noninvasive biological markers of hippocampal tissue microstructural organization (beyond the study of volumes) in animal studies across pathologies. Changes in tensor-derived measures in the CA1 and DG subfields of the hippocampus have been related to several gray matter insults in mouse models of amyloid accumulation (Whittaker et al., 2018; Daianu et al., 2015), status epilepticus (Salo et al., 2017), early life stress (Molet et al., 2016), and hippocampal sclerosis (Crombe et al., 2018), and indicate change on a cellular level. Importantly, dMRI metrics do not reflect cell-type specificity nor does dMRI currently have the resolution to observe diffusion at a single-cell level. Instead, dMRI metrics indicate difference among different types of tissue. Here our use of the terms microstructure and microstructural properties refer to the ability of dMRI to measure tissue differences within each voxel.

In humans, the use of dMRI measures as sensitive markers of hippocampal integrity in aging, mild cognitive impairment, and Alzheimer's Disease has been studied, however, has only scarcely been applied to hippocampal subfields possibly due to image resolution or the use of whole hippocampus instead of subfield anatomical segmentation (Colon-Perez et al., 2015; Dyrba et al., 2015; Kantarci et al., 2005; Mak et al., 2017; Muller et al., 2007; Reas et al., 2017). We have previously shown that the use of ultrahigh resolution dMRI in humans can uncover in vivo microstructural properties of white matter that are otherwise impossible to visualize using sequences with standard image resolutions (Yassa et al., 2010). Thus, it is possible that the use of ultrahigh resolution dMRI in humans is critical to uncover new and robust biomarkers of microstructural properties of gray matter within the MTL and hippocampal subfields that are not otherwise palpable using standard image resolutions.

In this investigation, we employ a state-of-the-art ultrahigh resolution dMRI sequence (0.67 mm × 0.67 mm × 3 mm) to quantify the microstructural features in MTL regions in a cohort of older adults (63–98 years old). Using diffusion tensor derived measures of mean diffusivity (MD) and fractional anisotropy (FA) we demonstrate the utility of this sequence by comparing its performance against a standard diffusion imaging sequence (1.7 mm isotropic). We assessed FA and MD in two hippocampal subfields (DG and CA1) and quantified relationships with age and episodic memory function, using a word list recall test (Rey Auditory Verbal Learning Test; RAVLT) that is often used to identify age-related memory impairment (Estévez-González et al., 2003). We also tested whether FA and MD in these subfields was related to performance on a spatial pattern separation task that is known to rely on the integrity of the DG (Marr et al. 1971; Yassa et al. 2011; Reagh et al., 2014). We focused on the DG and CA1 as they are both critical for episodic memory processes and are known to be impacted by aging and AD (Burger, 2010; Ianov et al., 2017; Small et al., 2004; Yassa et al., 2010).

2 | RESULTS

2.1 | Ultrahigh-resolution diffusion MRI detects subregion-specific gray matter diffusion profiles

We first tested the hypothesis that the ultrahigh resolution dMRI approach (0.67 × 0.67 × 3 mm^3) will reveal microstructural features of hippocampal subfields and rhinal cortical subregions that would be otherwise indiscernible using traditional diffusion imaging methods. We used k-means clustering to compute and label clusters of FA and MD values from the hippocampus (CA1 and DG), rhinal cortex, and collateral sulcus (the latter as a control). Using data derived from the ultrahigh-resolution sequence, we calculated the overlap between the labels derived from k-means clustering and known anatomical labels (CA1, DG, rhinal cortex, or sulcus). We obtained a normalized mutual information (nMI) score of 0.623, indicating a moderate overlap in the k-means cluster label (Figure 1b) and known anatomical label (Figure 1a). To determine whether these regions were differentiated by their FA values, we compared regional FA values CA1, DG, rhinal cortex, and sulcus using one-way ANOVA. We found a significant difference across regions ($F_{2,308} = 700.8$, $p < .0001$). Tukey's multiple comparison test revealed each region contained significantly different FA values than the other (Figure S1a). Similarly, we compared MD values in each of the same regions and found a significant difference across regions ($F_{3,308} = 342.3$, $p < .0001$). Tukey's multiple comparisons revealed that each region contained unique MD values except for MD values of the CA1 and rhinal cortex (adjusted $p = 0.99$; Figure S1b). These analyses demonstrate that the MTL regions could be discerned based on their microstructural properties, agnostic to their anatomical label.

To determine whether the same information could be gleaned from traditional whole brain DWI imaging, we repeated the same analyses as above with 1.7 mm isotropic data acquired during the same sessions for the same participants. The overlap between the labels derived from k-means clustering and known anatomical labels resulted in a nMI score of 0.242 indicating very minimal overlap between K-means cluster identity (Figure 1d) and known anatomical identity (Figure 1c). Similarly, we tested weather these regions were differentiated by their FA values. One-way ANOVA revealed a significant difference between regions ($F_{3,300} = 95.96$, $p < .0001$), however post-hoc analysis revealed that FA values derived from the CA1 were not statistically different than FA values of the rhinal cortex (adjusted
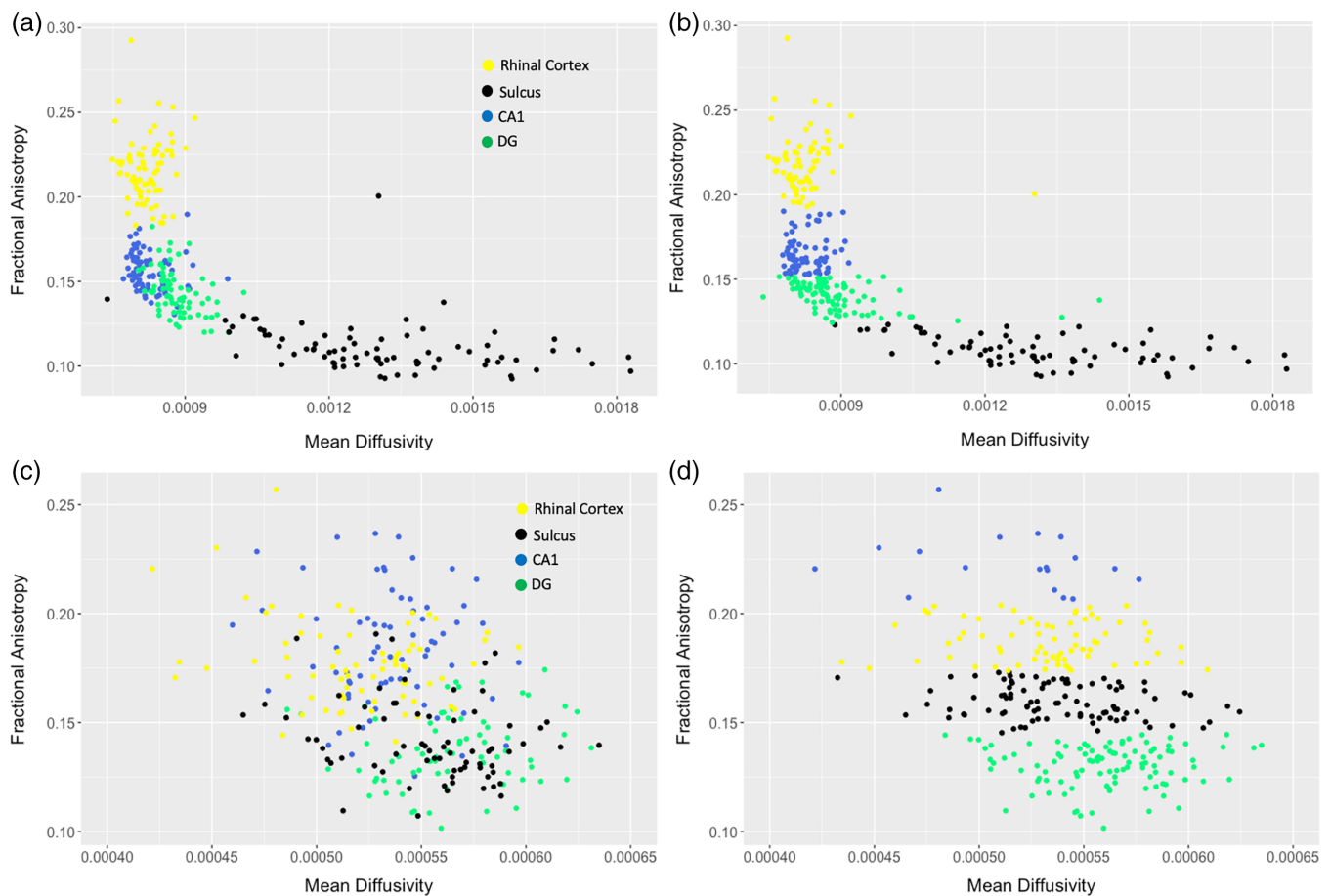
FIGURE 1 (a) Shows the FA and MD data for each area of interest: CA1 (in blue), DG (in green), rhinal cortex (in yellow), and sulcus (in black) derived from the *high-resolution DWI sequence*. (b) Shows the same data points categorized into four clusters via unsupervised K-means clustering. We note the large degree of visual overlap (normalized mutual information score = 0.623). (c) Shows the actual FA and MD data plotted for each area of interest: CA1 (in blue), DG (in green), rhinal cortex (in yellow), and sulcus (in black) derived from the *whole brain DWI sequence*. (d) Shows the same data points clustered into four clusters using unsupervised K-means clustering. Here we note the minimal degree of overlap between the actual data and predicted data identities (normalized mutual information score = 0.242)

$p = .99$, Figure S1c). We then compared MD values in each of the same regions and found significant difference across regions ($F_{3,304} = 50.71$, $p < .0001$), however, post-hoc analyses revealed that MD values derived from the CA1 were not statistically different than MD valued derived from the DG (adjusted $p = .93$, Figure S1d).

2.2 | Higher MD and lower FA in the DG are associated with increased age

We then asked if these microstructural properties derived from the ultrahigh resolution dMRI were associated with increasing age. In the DG, we found a negative association between age and FA (Pearson $r = -0.47$, $p < .0001$; Figure 2c), as well as positive association between age and MD (Pearson $r = 0.66$, $p < .0001$; Figure 2d). In the CA1, we found a significant positive association between age and MD (Pearson $r = 0.52$, $p < .0001$; Figure 2b). The

relationship between age and CA1 FA was not significant (Pearson $r = -0.13$, $p = .26$; Figure 2a).

Importantly, we note that our sample contains a bimodal distribution of age as data were collected from two cohorts (63–86 and 90–98 years old). To ensure that our findings were not driven by one particular age group, we assessed the difference in the slope of the relationship between age and the diffusion measures reported above across the two age groups. As a result, we investigated the relation between age and DG MD, age and DG FA, and age and CA1 MD within each age range separately. We found that there was no difference ($Z = -0.96$, $p = .34$) between the slope of the relation between age and DG MD in the young cohort ($\beta = 1.50 \times 10^{-6}$, $p = .023$) compared to the slope of the relation in the old cohort ($\beta = 5.73 \times 10^{-6}$, $p = .20$). We found no difference ($Z = -0.34$, $p = .74$) between the slope of the relation between age and DG FA in the young cohort ($\beta = -.00095$, $p = .0014$) and the slope of the relation between age and DG FA in
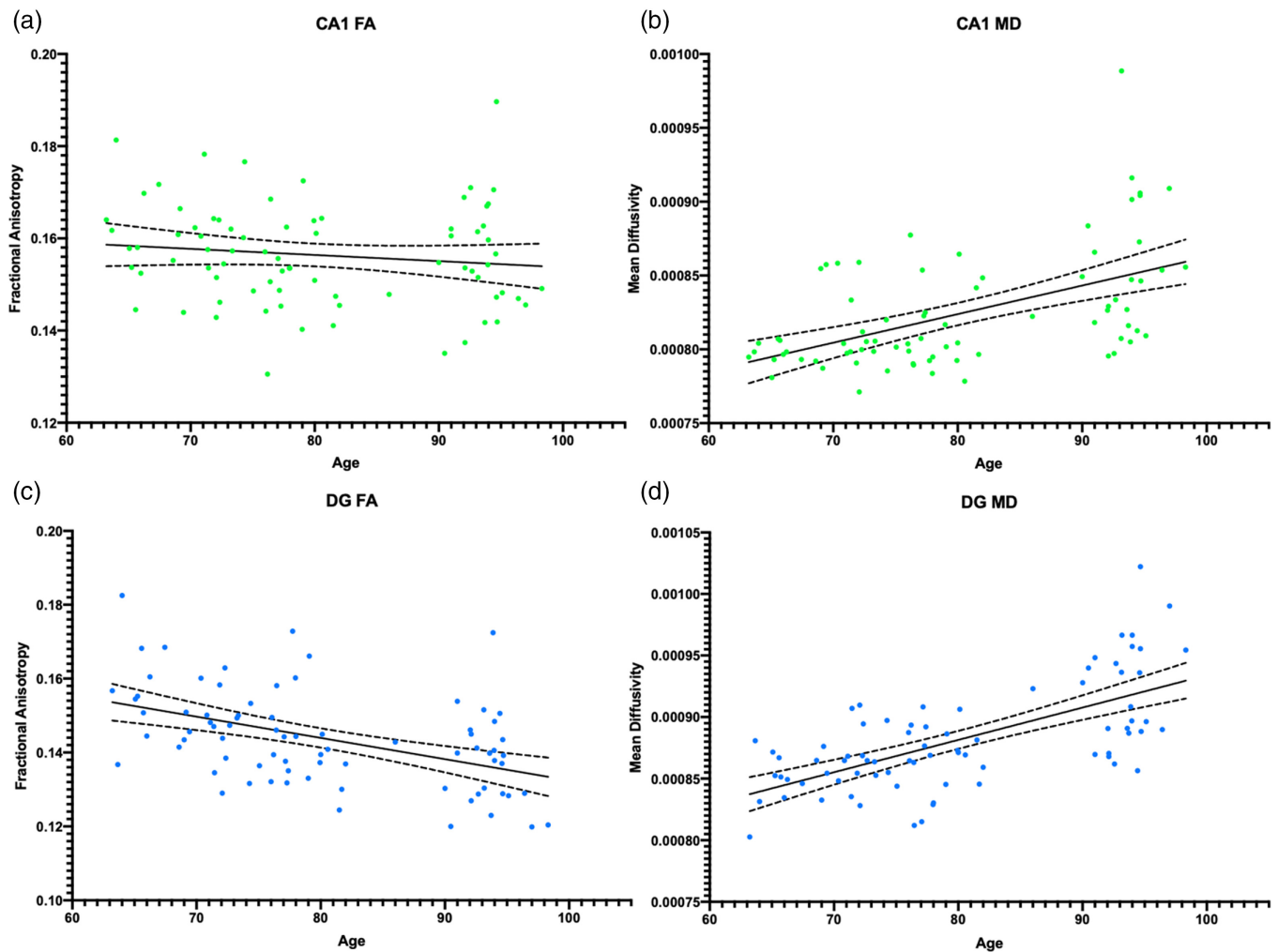
FIGURE 2 (a, b) Shows the results of CA1 structural differences across the age range. (c, d) Show the results of DG structural differences across the age range. (a) Shows the nonsignificant relation between age and CA1 FA ($r = -0.13$, $p = .26$). (b) Shows the positive relation between age and CA1 MD ($r = 0.52$, $p < .0001$). (c) Shows the negative association between age and DG FA ($r = -0.47$, $p < .0001$). Finally, (d) shows the positive relation between age and DG MD ($r = 0.66$, $p < .0001$)

the old cohort ($\beta = -.001386$, $p = .2834$). Similarly, we found no difference ($Z = -0.75$, $p = 0.45$) between the slope of the relation between age and CA1 MD ($\beta = 8.52 \times 10^{-7}$, $p = .18$) compared to the slope of the relation in the old cohort ($\beta = 4.49 \times 10^{-6}$, $p = .36$). These analyses are further described in Figure S2.

2.3 | Increased DG MD predicts worse performance on word list delayed recall

Aging is associated with episodic memory decline (Burke & Barnes, 2006; Levine et al., 2002; Mark & Rugg, 1998). In particular, the Rey Auditory Verbal Learning Test (RAVLT) delayed recall measure has been used in the past to assess general hippocampal integrity with age (Rey, 1964; Estevez-Gonzalez et al., 2003; Jedynak et al., 2012). We tested the hypothesis that increased DG MD and decreased FA would predict age-related impairments in RAVLT delayed recall performance. We found that DG MD (Pearson

$r = -0.54$, $p < .0001$; Figure 3a) was a significant predictor of delayed recall, however, DG FA was borderline (Pearson $r = 0.21$, $p = .064$; Figure 3b). To ensure that these effects are not driven by in-scanner head motion, we assessed whether average Euclidean distance moved during the ultrahigh-resolution scan was associated with DG MD and found the effect to be not significant (Pearson $r = 0.16$, $p = .16$; Figure S3). To ensure that these effects were not driven by DG volume we asked if DG MD predicted delayed recall performance while regressing out the effects of DG volume. We found that DG MD ($\beta = -.393$, $p = .00025$) was associated with delayed recall performance accounting for DG volume ($\beta = .32$, $p = .0021$). Although, we note that DG MD and DG volume are related to one another ($r = 0.45$, $p < .0001$).

To assess the impact of confounding variables such as age and sex, we used multiple regression with age, sex, and DG MD as predictors and RAVLT delayed recall as the outcome. We found that both age ($\beta = -.42$, $p = .00066$) and DG MD ($\beta = -.26$, $p = .030$) were independent predictors of delayed recall. Sex was not a significant
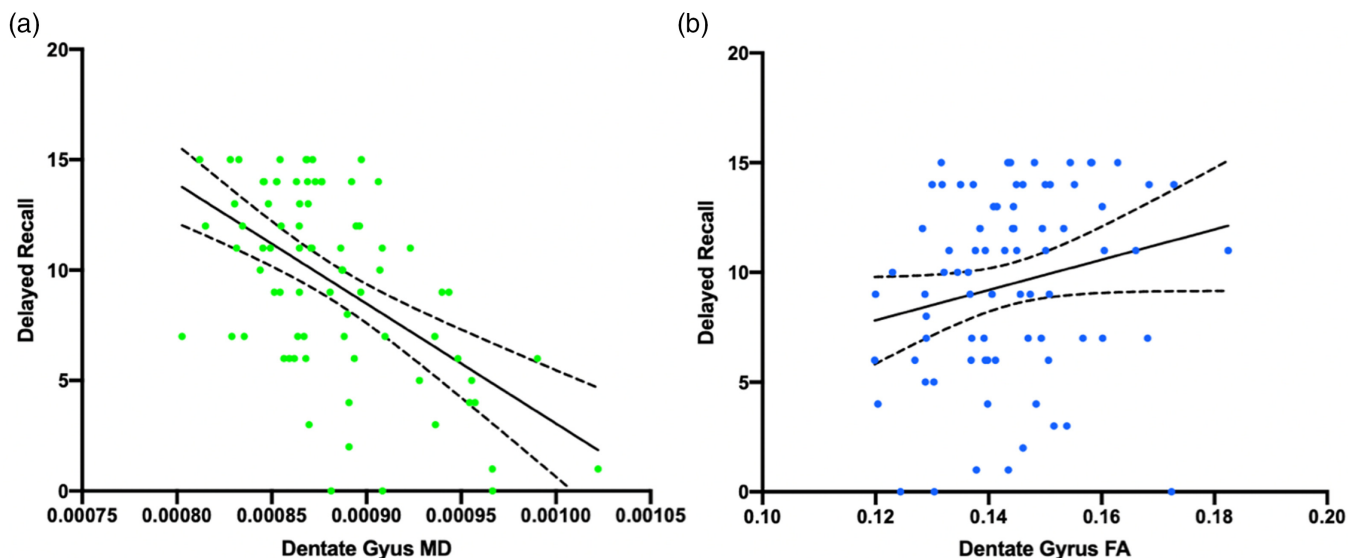
(a)

(b)

FIGURE 3 Here we report the results of DG MD, FA, and volume predicting delayed recall performance. (a) Shows the significant association between DG MD and delayed recall performance ($r = -0.54$, $p < .0001$). (b) Shows the nonsignificant but trending relation between DG FA and delayed recall performance ($r = 0.21$, $p = .064$)
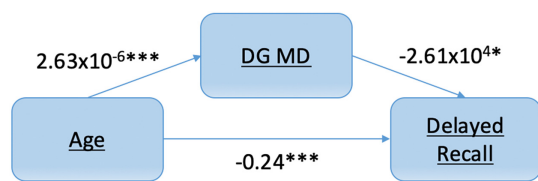

FIGURE 4 Results of structural equation (mediation) model shows DG MD is a statistically significant mediator between age and delayed recall performance (indirect effect = −0.069*, CI = −0.13– −0.0082). *indicated $p < .05$, ** indicates $p < .01$, *** indicates $p < .0001$

predictor, although the effect was borderline or trending towards significance ($\beta = -.15$, $p = .098$). Given the correlated structure across age, DG MD, and delayed recall performance, we conducted mediation analyses in an effort to understand whether changes in DG MD are a neurobiological mechanism that mediates the relationship between age and episodic memory performance. We found that DG MD mediated the relationship between age and RAVLT delayed recall. The bootstrapped unstandardized indirect effect was −0.069 and the 95% confidence interval ranged from −0.13 to −0.0082. The indirect effect was statistically significant ($p = .029$; Figure 4). This result suggests that increased DG MD may serve as a mechanistic biomarker for age-related episodic memory decline.

2.4 | Higher DG MD predicts worse performance on a spatial pattern separation task

While the RAVLT can be used to assess general episodic memory and has been used to index hippocampal function more broadly, the DG is

specifically associated with pattern separation, a neurocomputational mechanism by the brain reduces overlap across experiences and store them as unique memories (Marr et al. 1971; Yassa et al. 2011). We have previously developed a spatial pattern separation task (Reagh et al., 2014) to assess age-related changes in spatial memory and demonstrated that it engages the hippocampal DG preferentially over other subfields (Reagh et al., 2018; Reagh & Yassa, 2014). This task was administered to a subset of the participants in the current study (n = 53). As in our prior work, the lure discrimination index (LDI) was used as the principal behavioral outcome measure of interest. We replicated our previous finding of decreased LDI as a function of age (Pearson $r = -0.32$, $p = .019$). We also show that target recognition (no spatial displacement) is associated with age (Pearson $r = -0.31$, $p = .022$). Next, we tested the relationship between DG MD and LDI and found that increased DG MD was associated with worse LDI (Pearson $r = -0.39$, $p = .0051$; Figure 5b), but not with target recognition (Pearson $r = -0.22$, $p = .12$). We then tested if DG volume was related to LDI, the relation between DG volume and LDI was not a statistically significant ($r = 0.12$, $p = .40$; Figure 5c). Similar to the RAVLT analysis, we asked if increased DG MD was a mediator of the relationship between age and LDI. We found a marginally significant effect whereby DG MD mediated the relationship between age and LDI (indirect effect = −0.0026, CI = −0.0063–0.00013, $p = .076$).

3 | DISCUSSION

There are four major findings of this study. First, we show that the ultrahigh resolution dMRI sequence outperforms the standard resolution whole brain dMRI sequence in detecting subtle microstructural differences between MTL regions. Second, we show that increased
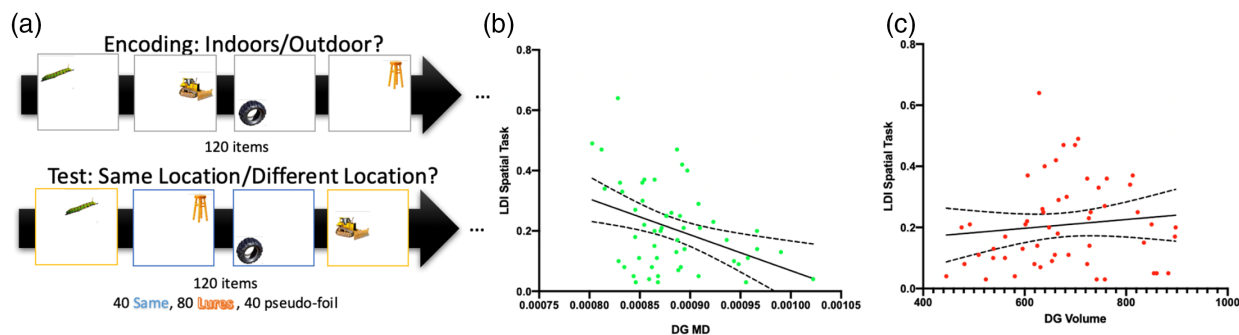
FIGURE 5 In a subset of participants, we tested whether DG MD might also predict performance on a spatial pattern separation task. (a) the spatial pattern separation task. During incidental encoding, subjects are shown a series of objects placed in different spatial locations on a screen. Subjects are asked during incidental encoding to rate the images as appearing as "indoor" or "outdoor". During test, targets or objects appearing in the same location as encoding are presented as well as lures which present the same objects in slightly different locations. Here subjects are asked if the object was in a "new location" or "old location". (b) There is a statistically significant association between DG MD and LDI on the spatial task ($r = -0.39$, $p = .0051$). (c) However, there is not a statistically significant association between DG volume and LDI ($r = 0.12$, $p = .40$)

age is associated with distinct microstructural changes within the CA1 (increased MD) and DG (decreased FA and increased MD). Third, we show that increased MD in the DG mediates the relationship between advanced age and episodic memory impairment. Finally, we provide evidence that DG MD derived from the ultrahigh-resolution sequence may offer critical information regarding the role of DG in spatial pattern separation. Overall, the approach described in this article provides enhanced sensitivity to regional microstructural differences in the MTL which enhances our ability to elucidate the neural mechanisms of age-related cognitive decline and AD.

We demonstrate that CA1, DG, and surrounding cortex have unique diffusion profiles and that the discrimination of these profiles is improved with the use of the ultrahigh resolution dMRI sequence. Our data-driven approach was able to more accurately cluster unlabeled FA and MD data points according to their true anatomical labels in the ultrahigh sequence compared to the standard isotropic resolution sequence. Interestingly, our evidence suggests that the CA1 and DG are dissociable based on measures of FA and MD derived from the ultrahigh-resolution sequence, but not the whole brain sequence. More specifically, we provide evidence that the CA1 and DG of the hippocampus contain different FA and MD values such that the CA1 contains greater FA and lesser MD compared to the DG. While direct histological evidence is needed to validate this claim, it is possible that the pyramidal cell layer contributes to greater FA in the CA1 as compared to the granule and mossy cells that constitute the DG (McKiernan et al., 2017; Amaral et al., 2007). Interestingly, the directionality of these signals is consistent with prior research in animals (Stolp et al., 2018) suggesting cross-species consistency of these profiles and that they might map onto cytoarchitectural and cellular differences within these regions (Stolp et al., 2018; Wu & Zhang, 2016). These analyses serve as a benchmark of the ability of ultrahigh resolution dMRI to differentiate between hippocampal structure and surrounding cortices using the collateral sulcus as an additional indicator.

Investigations attempting to dissociate hippocampal subfields based on diffusion profiles have predominantly been done in rodents and have been to some extent related to histological tissue properties (Stolp et al., 2018; Wu & Zhang, 2016). In humans, possibly due to resolution limitation (Colon-Perez et al., 2015), investigations have mainly studied diffusion properties of the hippocampus as a whole (Mak et al., 2017; Reas et al., 2017) with only a few studies segmenting hippocampal body into either anterior/posterior segments (Fjell et al., 2019) or along the head and tail (Hong et al., 2010). A few investigations have probed hippocampal subfield diffusion properties as they relate to aging and memory processes in vivo, however, these approaches had not been benchmarked for sensitivity to subfield differences (Radhakrishnan et al., 2020; Yassa et al., 2011). However, one study using data derived from the Human Connectome Project implemented nonnegative matrix factorization to identify components or groupings of similar FA and MD values of the MTL (Patel et al., 2020). Using this method, they were able to identify numerical partitions of the MTL that contain clusters of similar MD and FA values; however, it is unclear how the identifiable partitions map onto known subfields of the hippocampus. Another study using the ADNI dataset investigated the use of diffusion imaging within subfields to improve the detection and prediction of AD using MD (as well as volumes) of hippocampal subfields, however they did not report subfield-specific patterns of association with cognitive performance (Hett et al., 2019). Our current work is distinct from past contributions in that it demonstrates clear subfield-specific diffusion feature profiles and provides evidence for subfield-specific features predictive of memory performance.

Ultrahigh resolution diffusion imaging has previously been used to quantify directional anisotropy in specific white matter pathways (e.g., the perforant path), which was not possible using traditional approaches (Yassa et al., 2010). In the current investigation we improved on this method by using the ZOOMit scan procedure which utilizes inner volume excitation to increase the in-plane resolution (Blasche et al., 2012) in a limited field of view (in this case positioned along the hippocampal axis) under the assumption that we might also be able to detect differences in gray matter microstructure that might

otherwise not be detectable. Variants of this sequence have primarily been used for imaging deep small organs including the prostate, spinal cord, pancreas, and optic nerve (Liney et al., 2015; Saritas et al., 2008; Seeger et al., 2018; Sim et al., 2020). Interestingly, only a handful of studies have implemented the ZOOMit sequence in brain tissue and have provided evidence of distinct advantages over their standard sequence counterparts. For instance, some evidence shows that the ZOOMit acquisition applied to BOLD contrast may be superior to conventional BOLD sequences in detecting hand-motor cortex (Fang et al., 2020). Additionally, the use of a structural ZOOMit sequence (paired with EEG) has been shown to facilitate localization of epileptic foci in patients whose focal cortical dysplasia went previously undetected using standard structural sequences (Aydin et al., 2017). Here, we demonstrate the utility and feasibility of this approach to identify hippocampal subfield-level microstructural property profiles, which was not possible with standard diffusion sequences, and further validate the approach using anatomical a-priori knowledge as well as by testing associations with hypothesized cognitive outcomes. The relevant main anatomical a priori knowledge used here is that the collateral sulcus would provide a diffusion profile consistent with nontissue (unrestricted free diffusion profile, hence lower FA and higher MD compared to tissue samples).

In addition to providing evidence of regionally specific diffusion properties, we show that increased MD within CA1 and increased MD and decreased FA in DG are associated with age. In this investigation, we note that the measures of FA and MD were calculated from within subject-specific subfield volumes, thus, changes of FA and MD inherently yield additional information regarding tissue microstructural organization across the aging spectrum that may supplement gross volumetric changes. In addition to showing an effect of age, we also show that DG volume and DG MD are associated with memory performance as assessed by the delayed recall portion of the RAVLT, relationships that persisted after accounting for age and sex. Additionally, our structural equation modeling analyses suggest that DG MD mediates the relationship between age and delayed recall performance, suggesting a putative mechanism for age-related episodic memory decline. While the cell type specificity in the interpretation of greater MD is unclear, this metric captures restricted diffusion and can generally be thought of as inversely related to "cellularity" or cellular density (Yeh et al., 2014). In other words, a smaller number of cells results in greater unrestricted diffusion (greater MD). While this could potentially signify cellular loss in the DG, which is consistent with the volumetric decline we also observe with age, this interpretation remains speculative.

The DG is thought to play an important role in the neurocomputational process known as pattern separation, or the process by which similar experiences are encoded using distinct memory traces (Yassa & Stark, 2011). Recently, we have shown that spatial pattern separation is compromised in aged-impaired groups (Reagh et al., 2014). To further probe DG function, we asked whether DG MD was related to performance on a spatial pattern separation challenge. Here, we provide evidence that increased DG MD is associated with impaired spatial pattern separation performance whereas DG volume was not. Unlike the RAVLT, pattern separation tasks tend to be specific to DG impairment (Leal and Yassa, 2015), thus this directed test of the relationship between DG MD and spatial pattern separation performance provides further specificity. It is important to note that the diffusion profiles observed and their relationships with memory measures occur in the absence of clinical dementia as this is a nondemented sample of older adults. Our results suggest that microstructural alterations in the DG may be a more sensitive biomarker of age-related memory loss than DG volume or overall hippocampal volume.

A limitation of this study is the use of tensor derived measures which are susceptible to partial volume effects and in gray matter can lead to difficulty in interpretation (Assaf, 2018; Alexander et al., 2007, Alexander et al., 2011; Jdabdi & Johansen-Berg, 2011). While our approach employing high in-plane resolution limits the degree of partial volume averaging compared to sequences of standard voxel resolution, the single tensor characterization of DTI is another source of volume averaging which we did not address with this work. Model-free reconstruction methods such as NODDI (Zhang et al., 2012) and ActiveAx (Alexander et al., 2011) have shown promise in alleviating the limitations of DTI and have successfully detected microstructural differences associated with amyloidosis (Colon-Perez et al., 2019) and aging pathology in humans in the hippocampus (Radhakrishnan et al., 2020; Reas et al., 2017). However, such model free methods typically require multiple b-shells, which was not the case with our ZOOMit acquisition. Future work using this ultrahigh resolution sequence may incorporate several diffusion weightings to probe microstructural integrity more thoroughly.

In addition, we note that in this investigation there were multiple differences in scan parameters across the ZOOMit dMRI sequence and whole brain dMRI sequence and the impact of these differences were not systematically evaluated. Indeed, the whole brain dMRI sequence is superior in terms of the number of sampling directions. Thus, we suggest that the high resolution of the ZOOMit sequence as well as its acquisition plane along the principal axis of the hippocampus could potentially serve to both limit partial volume effects and enhance the spatial fitting of ASHS regions to the native diffusion space. Future work is needed to systematically investigate how differences in number of nondiffusion weighted images, number of diffusion weighted images, b-value, scan resolution, and acquisition plane may impact the quantification of hippocampal subfield diffusion profiles and their association with age-related cognitive decline. In addition, we note in this investigation *eddy_correct* was used rather than *eddy*, future research should seek to both preprocess high resolution data with *eddy* as well as to implement opposite phase encoding in order to correct for magnetization induced susceptibility distortions.

Finally, it is possible that slight differences in the alignment of the ZOOMit FOV during acquisition could have some impact on these results. While we took measures to mitigate operator differences in FOV alignment along the hippocampus with standard operator protocols and training we note that this possibility is not completely excluded.

	Full sample	Young-old	Oldest-old
N	78	52	26
Sex	Female 54 Male 24	Female 38 Male 14	Female 16 Male 10
Age	80.18 ± 10.61 (Range 63.22–98.31)	73.48 ± 5.56 (Range 63.22–86.00)	93.59 ± 1.95 (Range 90–98.31)
Years of education	16.18 ± 2.50	16.58 ± 2.22	15.38 ± 2.87
Cognitive impairment[a]	9 CIND	0 CIND	9 CIND
RAVLT delayed recall	9.46 ± 4.26	11.42 ± 3.21	5.54 ± 3.31
Mini mental state exam	27.28 ± 2.45	28.15 ± 1.42	25.54 ± 3.10
Completed SPS task	53	36	17
CDR sum of boxes	$n = 66$ 0.12 ± 0.35 Range (0.0–2.0)	$n = 40$ 0.025 ± 0.11 Range (0.0–0.5)	$n = 26$ 0.27 ± 0.51 Range (0.0–2.0)

[a]CIND–cognitive impairment no dementia.

In conclusion, we have shown using the ZOOMit ultrahigh resolution dMRI sequence that hippocampal subfields contain unique and dissociable diffusion properties. We have shown that these diffusion properties become compromised with increased age and compromised integrity of the DG may mediate the link between age and impaired episodic memory function.

4 | METHODS

4.1 | Participants

Participants were recruited from two separate cohorts (Young-Old and Oldest-Old) at the University of California, Irvine to allow us to examine a large range of ages from 60–100 for a total sample of 78 participants (54 female, mean age 80.18). Demographic and cognitive performance data of the two cohorts are summarized in Table 1. Recruitment criteria for the Young-Old (age range 63–86) included being between the ages of 60 and 86, speak fluent English, had adequate visual and auditory acuity for neuropsychological and computerized testing, good health with no disease(s) expected to interfere with the study, willing and able to participate for the duration of the study and in all study procedures including MRI, and had normal cognition defined as a Clinical Dementia Rating of 0 and Mini-Mental State Examination Score of 27 or higher. All procedures were in accordance with protocols approved by the UC Irvine Institutional Review Board. Recruitment criteria for the Oldest-Old (age range 93–98) was largely the same, except for testing visual and auditory acuity and the MMSE cutoff. Oldest-Old participants were screened for visual and auditory impairment as part of initial medical screening. We note that roughly one-third (NINE participants) were diagnosed with Cognitive Impairment with No Dementia (CIND) and the average MMSE score for the Oldest-Old was lower than the Young-Old (25.54 compared to 28.15). For reference, we also report scores on the Clinical Dementia Rating Scale Sum of Boxes (CDR Sum of Boxes). Twelve participants from the Young-Old cohort did not complete CDR.

4.1.1 | MR image acquisition

All neuroimaging data were acquired on a 3.0 Tesla Siemens Prisma scanner at the Facility for Imaging and Brain Research (FIBER) at the University of California, Irvine. A high-resolution 3D magnetization-prepared rapid gradient echo (MPRAGE) structural scan (0.8 mm isotropic voxels) was acquired at the beginning of each session: repetition time (TR) = 2300 ms, echo time (TE) = 2.38 ms, FOV = 192, 256, 256 mm, flip angle = 8°. In addition, a T2-weighted high-resolution hippocampal sequence was acquired: TR/TE = 5000/84 ms, flip angle = 17°, FOV = 190, 105, 198 mm, voxel size = $0.42 \times 0.42 \times 2.4$ mm^3. The ultrahigh-resolution diffusion sequence was collected as oblique coronal slices parallel to the principal axis of the hippocampus with the following parameters: TR/TE = 3500/75 ms, FOV = 180, 71, 66 mm, voxel size = $0.67 \times 0.67 \times 3$ mm^3, bandwidth = 1696 Hx/Px, echo spacing = 0.69 ms, EPI factor = 40, TX acceleration = 2.0, total approximate run time = 3 min 42 s. These parameters were optimized by Siemen's scanner interface. The sequence consisted of two b = 0 s/mm^2 volumes and a total of 60 diffusion weighted volumes acquired as 30 noncollinear directions repeated twice at a b-value of 1000 s/mm^2. This sequence (ZOOMit) utilizes inner volume excitation to reduce the field of view and in-plane resolution (Blasche et al., 2012). Here we oriented the FOV of the ZOOMit sequence along the long axis of the hippocampus in hopes to more accurately sample MTL tissue. Upon acquiring the MPRAGE image, trained scanner technicians placed the bottom edge of the square FOV "ON" or along the hippocampal body from a sagittal view. The center of the box was then placed over the hippocampus to cover the entire body of the hippocampus. The MPRAGE was checked to ensure that the FOV covered both the left and right hippocampus in its entirety. In this manner, by orienting the FOV along the hippocampus, we hope to minimize partial volume effects across regions given the 3 mm slice thickness projects within hippocampal layers rather than across hippocampal layers. More information on this protocol as well as example MPRAGE and T2-weighted images are supplied in Figure S4. A whole brain diffusion sequence was also acquired with the following parameters: TR/TE = 3500/102 ms, FOV = 218, 221, 189 mm, voxel

size = 1.7 mm isotropic, bandwidth = 1698 Hz/Px, echo spacing = 0.71 ms, EPI factor = 110, total approximate run time = 8 min and 6 s. The sequence consisted of 7 b = 0 s/mm^2 volumes and two b-values of 1500 s/mm^2, 3000 s/mm^2 each with 64 diffusion weighted volumes. To make the ZOOMit and whole brain sequence more comparable, we removed all volumes where b = 3000 s/mm^2 from the whole brain sequence. All vector orientations were automatically generated by Siemen's Prisma software.

4.1.2 | Medial temporal lobe subfield segmentation in native diffusion space

We parsed the subfields of the MTL using T1 and T2-weighted images and the Automated Segmentation of Hippocampal Subfields (ASHS; Yushkevich et al., 2014) pipeline to automatically label the T2-weighted images. This method implements joint label fusion and correcting learning and is a highly accurate method in automatically deriving hippocampal subfield volumes and cortical subregions in the MTL. Using ASHS, we calculated the volumes for the following subregions bilaterally in native T2 space: CA1, CA2, CA3, DG, subiculum, sulcus, BA35, BA36, and PHC. For all volumetric analyses, volumes were averaged across hemisphere. To query microstructural differences beyond volume, we used the ANTSRegistrationSyn program offered by Advanced Normalization Tools (ANTS; Avants et al., 2011; Klein et al., 2009) to warp the T2 and associated ASHS regions into the first B0 of the partial FOV ultrahigh-resolution diffusion sequence (Figure S5) as well as the first B0 of the whole brain diffusion scan. We preprocessed both the high-resolution sequence and whole brain sequence using eddy_correct. We quantified motion by calculating the average Euclidian distance in the linear transformation from each subbrick to the first B0 volume prior to any motion correction for each dMRI scan.

4.1.3 | Computation of tensor-based metrics

We calculated FA and MD maps using FSL's DTIfit. Fractional anisotropy and MD values for each MTL subfield (bilaterally) from ASHS output were calculated and averaged across hemispheres using AFNIs 3dmaskave command. This process was completed for both the ultrahigh resolution dMRI sequence and the whole brain dMRI sequence. For dissociating tissue from nontissue samples, we compared the sulcus, CA1, DG, and rhinal cortex (defined as averaging BA35, BA36, ERC, and PHC). One subject was removed from the MD whole brain analysis and two subjects were removed from the FA whole brain analysis as clear outliers.

4.1.4 | Neuropsychological testing

Our primary outcome measure in this investigation was performance on the Rey Auditory Verbal Learning Memory Test (RAVLT; Rey, 1964) to measure the acuity of verbal memory. Administration of the RAVLT consisted of an examiner reading a list of 15 words, after which the

subject was asked to repeat as many words as they could remember (in any order). This study/test trial was be repeated for a total of five learning trials (Learning Trials, A1-A5) that were then followed by an immediate recall of a distractor list (B1), then immediate recall of the original list of 15 words (Immediate Recall, A6). The subject was then tested 20 min later (Delayed Recall, A7), followed by a recognition test. The RAVLT and delayed recall component is a well-established benchmark for testing and dissociating normal aging, MDI, and Alzheimer's Disease (Estevez-Gonzalez et al., 2003; Jedynak et al., 2012).

4.1.5 | Spatial pattern separation task

In a subset of participants (n = 53, Table S1), we administered the spatial pattern separation task (Figure 5a) to probe DG function specifically. This task has been used previously to assess dentate-gyrus dependent pattern separation (Reagh et al., 2014). During incidental encoding, subjects were asked to rate objects as either 'Indoor' or 'Outdoor' as objects appeared in various positions on the screen. For the Young-Old cohort, each trial lasted 2.5 s with a 0.5 s ISI. In the Oldest-Old cohort, each trial was self-paced due to concerns regarding motor speed. The Oldest-Old cohort was instructed to respond as soon as they were able. For both cohorts, 160 items were presented during incidental encoding. During test, 40 target images (objects appearing in the same location as encoding), 80 lures (same objects in slightly different locations), and 40 pseudo-foil images (objects originally presented in one corner location at study and in another corner location at test) were presented. Lure images were binned as either large move (low similarity, 40 images) or small move (high similarity, 40 images). Pseudo-random images were the only set to appear in the corners of the screen. During test, participants were asked if the object was in the "Old Location" or in a "New Location". We quantified a Lure Discrimination Index (LDI) for highly similar lure items which measures performance on the task accounting for response bias: P("New Location"|Lure) – P("New Location"|Target) and did not consider the pseudo-foil images in these analyses. This measure is frequently employed as it not only accounts for response bias but is also sensitive to changes in aging (Reagh et al., 2018; Reagh et al., 2014; Stark et al., 2015). Here we chose the high-similarity lure bins under the assumption that the ability to adjudicate between stimuli with greater interference (greater similarity) would be more sensitive to aging. We excluded participants who could not respond to more than 75% of the test phase of the task. Additionally, all participants who had a negative LDI were eliminated under the assumption of the response being entirely driven by response bias or inattention to the task instructions. Exclusion based on these criteria let to a final subsample of 53 participants.

4.2 | Statistical analysis

Statistical analyses were computed using a mixture of Prism 7, R-Studio Software, and Python. K-means clustering was

implemented using Python using *sklearn.cluster* to identify 4 clusters (selected a priori), with a random state initialization of 0. Normalized mutual information scores were calculated in Python to compare the known identities of regions with the clusters identified from K-means. Regression models were completed using R-Studio Software and standardized beta coefficients are reported in-text. All correlational analyses were done using two-tailed tests of Pearson correlation coefficients. To assess the impact of the bimodal distribution of age on measures of DG MD and DG volume, we compared the slopes of DG MD and DG volume using a simple test of slopes. Mediation analyses were conducted using the *mediation* package in R, each model was tested using bias corrected and accelerated (BCa) bootstrapping with 5000 replications.

AUTHOR CONTRIBUTIONS

Steven J. Granger, Claudia H. Kawas, and Michael A. Yassa designed the research, Steven J. Granger, Myra Saraí Larson, Mithra T. Sathishkumar, Anna P. Smith, Liv McMillan, Dana Greenia, and Maria M. Corrada performed the research, Luis Colon-Perez, John T. Janecek, Michael Phelan and David B. Keator contributed analytic tools, Steven J. Granger analyzed data, Steven J. Granger drafted the initial version of the paper, Steven J. Granger and Michael A. Yassa wrote the paper with input from all of the authors.

ACKNOWLEDGMENTS

DATA AVAILABILITY STATEMENT

The data that support the findings of this study are available from the corresponding author upon reasonable request.

ORCID

Luis Colon-Perez https://orcid.org/0000-0001-8918-2418
Myra Saraí Larson https://orcid.org/0000-0001-5487-4828
Michael A. Yassa https://orcid.org/0000-0002-8635-1498

REFERENCES

Alexander, A. L., Hurley, S. A., Samsonov, A. A., Adluru, N., Hosseinbor, A. P., Mossahebi, P., do Tromp, P. M., Zakszewski, E., & Field, A. S. (2011). Characterization of cerebral white matter properties using quantitative magnetic resonance imaging stains. *Brain Connectivity*, 1, 423–446.

Alexander, A. L., Lee, J. E., Lazar, M., & Field, A. S. (2007). Diffusion tensor imaging of the brain. *Neurotherapeutics: the journal of the American Society for Experimental Neuro Therapeutics*, 4, 316–329.

Amaral, D. G., Scharfman, H. E., & Lavenex, P. (2007). The dentate gyrus: Fundamental neuroanatomical organization (dentate gyrus for dummies). *Progress in Brain Research*, 163, 3–22.

Assaf, Y. (2018). Imaging laminar structures in the gray matter with diffusion MRI. *NeuroImage*, 197, 677–688.

Avants, B. B., Tustison, N. J., Song, G., Cook, P. A., Klein, A., & Gee, J. C. (2011). A reproducible evaluation of ANTs similarity metric performance in brain image registration. *NeuroImage*, 54, 2033–2044.

Aydin, Ü., Rampp, S., Wollbrink, A., Kugel, H., Cho, J., Knösche, T. R., Grova, C., Wellmer, J., & Wolters, C. H. (2017). Zoomed MRI guided by combined EEG/MEG source analysis: A multimodal approach for optimizing Presurgical epilepsy work-up and its application in a multifocal epilepsy patient case study. *Brain Topography*, 30(4), 417–433.

Blasche, M., Riffel, P., & Lichy, M. (2012). TimTX TrueShape and syngo ZOOMit technical and practical aspects. *Magnetom Flash*, 1, 74–84.

Braak, H., & Braak, E. (1991). Neuropathological stageing of Alzheimer-related changes. *Acta Neuropathologica*, 82, 239–259.

Burger, C. (2010). Region-specific genetic alterations in the aging hippocampus: Implications for cognitive aging. *Frontiers in Aging Neuroscience*, 2, 140.

Burke, S. N., & Barnes, C. A. (2006). Neural plasticity in the ageing brain. *Nature Reviews. Neuroscience*, 7(1), 30–40.

Colon-Perez, L. M., Ibanez, K. R., Suarez, M., Torroella, K., Acuna, K., Ofori, E., Levites, Y., Vaillancourt, D. E., Golde, T. E., Chakrabarty, P., & Febo, M. (2019). Neurite orientation dispersion and density imaging reveals white matter and hippocampal microstructure changes produced by Interleukin-6 in the TgCRND8 mouse model of amyloidosis. *NeuroImage*, 202, 116138.

Colon-Perez, L. M., King, M., Parekh, M., Boutzoukas, A., Carmona, E., Couret, M., Klassen, R., Mareci, T. H., & Carney, P. R. (2015). High-field magnetic resonance imaging of the human temporal lobe. *NeuroImage. Clinical*, 9, 58–68.

Crombe, A., Planche, V., Raffard, G., Bourel, J., Dubourdieu, N., Panatier, A., Fukutomi, H., Dousset, V., Oliet, S., Hiba, B., & Tourdias, T. (2018). Deciphering the microstructure of hippocampal subfields with in vivo DTI and NODDI: Applications to experimental multiple sclerosis. *NeuroImage*, 172, 357–368.

Csernansky, J. G., Wang, L., Joshi, S., Miller, J. P., Gado, M., Kido, D., McKeel, D., Morris, J. C., & Miller, M. I. (2000). Early DAT is distinguished from aging by high-dimensional mapping of the hippocampus. *Dementia of the Alzheimer type. Neurology*, 55(11), 1636–1643.

Csernansky, J. G., Wang, L., Swank, J., Miller, J. P., Gado, M., McKeel, D., Miller, M. I., & Morris, J. C. (2005). Preclinical detection of Alzheimer's disease: Hippocampal shape and volume predict dementia onset in the elderly. *NeuroImage*, 25(3), 783–792.

Daianu, M., Jacobs, R. E., Weitz, T. M., Town, T. C., & Thompson, P. M. (2015). Multi-shell hybrid diffusion imaging (hydi) at 7 tesla in tgf344-ad transgenic Alzheimer rats. *PLoS One*, 10(12), 1–18.

Dillon, S. E., Tsivos, D., Knight, M., Mccann, B., Shiel, A. I., Conway, M. E., Newson, M. A., Kauppinen, R. A., & Coulthard, E. J. (2017). The impact of ageing reveals distinct roles for human dentate gyrus and CA3 in pattern separation and object recognition memory. *Scientific Reports*, 7, 1–13.

Dyrba, M., Barkhof, F., Fellgiebel, A., Filippi, M., Hausner, L., Hauenstein, K., Kirste, T., & Teipel, S. J. (2015). EDSD study group. Predicting prodromal Alzheimer's disease in subjects with mild cognitive impairment using machine learning classification of multimodal multicenter diffusion-tensor and magnetic resonance imaging data. *Journal of Neuroimaging*, 25(5), 738–747.

Estévez-González, A., Kulisevsky, J., Boltes, A., Otermin, P., & García-Sánchez, C. (2003). Rey verbal learning test is a useful tool for differential diagnosis in the preclinical phase of Alzheimer's disease: Comparison with mild cognitive impairment and normal aging. *International Journal of Geriatric Psychiatry*, 18, 1021–1028.

Fang, S., Bai, H. X., Fan, X., Li, S., Zhang, Z., Jiang, T., & Wang, Y. (2020). A novel sequence: ZOOMit-blood oxygen level-dependent for motor-cortex localization. *Neurosurgery*, 86(2), E124–E132.

Fjell, A. M., Sneve, M. H., Sederevicius, D., Sørensen, Ø., Krogsrud, S. K., Mowinckel, A. M., & Walhovd, K. B. (2019). Volumetric and microstructural regional changes of the hippocampus underlying development of recall performance after extended retention intervals. *Developmental Cognitive Neuroscience*, *40*, 100723.

Fox, N. C., & Freeborough, P. A. (1997). Brain atrophy progression measured from registered serial MRI: Validation and application to Alzheimer's disease. *Journal of Magnetic Resonance Imaging*, *7*, 1069–1075.

Frisoni, G. B., Fox, N. C., Jack, C. R., Scheltens, P., & Thompson, P. M. (2010). The clinical use of structural MRI in Alzheimer disease. *Nature Reviews. Neurology*, *6*, 67–77.

Gomez-Isla, T., Price, J. L., McKeel, D. W. J., Morris, J. C., Growdon, J. H., & Hyman, B. T. (1996). Profound loss of layer II entorhinal cortex neurons occurs in very mild Alzheimer's disease. *Neuroscience*, *16*, 4491–4500.

Hett, K., Ta, V. T., Catheline, G., Tourdias, T., Manjón, J. V., Coupé, P., & Alzheimer's Disease Neuroimaging Initiative. (2019). Multimodal hippocampal subfield grading for Alzheimer's disease classification. *Scientific Reports*, *9*(1), 13845.

Hong, Y. J., Yoon, B., Shim, Y. S., Cho, A. H., Lim, S. C., Ahn, K. J., & Yang, D. W. (2010). Differences in microstructural alterations of the hippocampus in Alzheimer disease and idiopathic normal pressure hydrocephalus: A diffusion tensor imaging study. *American Journal of Neuroradiology*, *31*(10), 1867–1872.

Ianov, L., De Both, M., Chawla, M. K., Rani, A., Kennedy, A. J., Piras, I., Day, J. J., Siniard, A., Kumar, A., Sweatt, J. D., Barnes, C. A., Huentelman, M. J., & Foster, T. C. (2017). Hippocampal transcriptomic profiles: Subfield vulnerability to age and cognitive impairment. *Frontiers in Aging Neuroscience*, *9*, 383.

Jack, C. R., Petersen, R. C., Xu, Y. C., O'Brien, P. C., Smith, G. E., Ivnik, R. J., Boeve, B. F., Waring, S. C., Tangalos, E. G., & Kokmen, E. (1999). Prediction of AD with MRI-based hippocampal volume in mild cognitive impairment. *Neurology*, *52*, 1397–1403.

Jbabdi, S., & Johansen-Berg, H. (2011). Tractography: Where Do we go from here? *Brain Connectivity*, *1*, 169–183.

Jedynak, B. M., Lang, A., Liu, B., Katz, E., Zhang, Y., Wyman, B. T., Raunig, D., Jedynak, C. P., Caffo, B., & Prince, J. L. (2012). A computational neurodegenerative disease progression score: Method and results with the Alzheimer's disease neuroimaging initiative cohort. *NeuroImage*, *63*, 1478–1486.

Kantarci, K., Petersen, R. C., Boeve, B. F., Knopman, D. S., Weigand, S. D., O'Brien, P. C., Shiung, M. M., Smith, G. E., Ivnik, R. J., Tangalos, E. G., & Jack, C. R. (2005). DWI predicts future progression to Alzheimer disease in amnestic mild cognitive impairment. *Neurology*, *64*(5), 902–904.

Klein, A., Andersson, J., Ardekani, B. A., Ashburner, J., Avants, B., Chiang, M. C., Christensen, G. E., Collins, D. L., Gee, J., Hellier, P., Song, J. H., Jenkinson, M., Lepage, C., Rueckert, D., Thompson, P., Vercauteren, T., Woods, R. P., Mann, J. J., & Parsey, R. V. (2009). Evaluation of 14 nonlinear deformation algorithms applied to human brain MRI registration. *NeuroImage*, *46*, 786–802.

Leal, S. L., & Yassa, M. A. (2015). Neurocognitive aging and the hippocampus across species. *Trends in Neurosciences*, *38*(12), 800–812.

Levine, B., Svoboda, E., Hay, J. F., Winocur, G., & Moscovitch, M. (2002). Aging and autobiographical memory: Dissociating episodic from semantic retrieval. *Psychology and Aging*, *17*(4), 677–689.

Liney, G. P., Holloway, L., Al Harthi, T. M., Sidhom, M., Moses, D., Juresic, E., Rai, R., & Manton, D. J. (2015). Quantitative evaluation of diffusionweighted imaging techniques for the purposes of radiotherapy planning in the prostate. *The British Journal of Radiology*, *88*(1049), 20150034.

Mak, E., Gabel, S., Su, L., Williams, G. B., Arnold, R., Passamonti, L., Rodriguez, P. V., Surendranathan, A., Bevan-Jones, W. R., Rowe, J. B., & O'Brien, J. T. (2017). Multi-modal MRI investigation of volumetric and microstructural changes in the hippocampus and its subfields in mild cognitive impairment, Alzheimer's disease, and

dementia with Lewy bodies. *International Psychogeriatrics*, *29*(4), 545–555.

Mark, R. E., & Rugg, M. D. (1998). Age effects on brain activity associated with episodic memory retrieval. An electrophysiological study. *Brain: A Journal of Neurology*, *121*(Pt 5), 861–873.

Márquez, F., & Yassa, M. A. (2019). Neuroimaging biomarkers for Alzheimer's disease. *Molecular Neurodegeneration*, *14*(1), 1–14.

Marr, D. (1971). Simple memory: A theory for archicortex. *Philosophical Transactions of the Royal Society B: Biological Sciences*, *262*, 23–81.

McKiernan, E. C., & Marrone, D. F. (2017). CA1 pyramidal cells have diverse biophysical properties, affected by development, experience, and aging. *PeerJ*, *5*, e3836.

Molet, J., Maras, P. M., Kinney-Lang, E., Harris, N. G., Rashid, F., Ivy, A. S., Solodkin, A., Obenaus, A., & Baram, T. Z. (2016). MRI uncovers disrupted hippocampal microstructure that underlies memory impairments after early-life adversity. *Hippocampus*, *26*(12), 1618–1632.

Muller, M. J., Greverus, D., Weibrich, C., Dellani, P. R., Scheurich, A., Stoeter, P., & Fellgiebel, A. (2007). Diagnostic utility of hippocampal size and mean diffusivity in amnestic MCI. *Neurobiology of Aging*, *28*(3), 398–403.

Ohm, T. G. (2007). The dentate gyrus in Alzheimer's disease. *Progress in Brain Research*, *163*, 723–740.

Patel, R., Steele, C. J., Chen, A. G. X., Patel, S., Devenyi, G. A., Germann, J., Tardif, C. L., & Chakravarty, M. M. (2020). Investigating microstructural variation in the human hippocampus using non-negative matrix factorization. *NeuroImage*, *207*, 116348.

Price, J. L., Ko, A. I., Wade, M. J., Tsou, S. K., McKeel, D. W., & Morris, J. C. (2001). Neuron number in the entorhinal cortex and CA1 in preclinical Alzheimer disease. *Archives of Neurology*, *58*, 1395–1402.

Radhakrishnan, H., Stark, S. M., & Stark, C. E. L. (2020). Microstructural alterations in hippocampal subfields mediate age-related memory decline in humans. *Front. Aging Neuroscience*, *12*, 1–15.

Reagh, Z. M., Noche, J. A., Tustison, N. J., Delisle, D., Murray, E. A., & Yassa, M. A. (2018). Functional imbalance of anterolateral entorhinal cortex and hippocampal dentate/CA3 underlies age-related object pattern separation deficits. *Neuron*, *97*, 1187–1198.

Reagh, Z. M., Roberts, J. M., Ly, M., DiProspero, N., Murray, E., & Yassa, M. A. (2014). Spatial discrimination deficits as a function of mnemonic interference in aged adults with and without memory impairment. *Hippocampus*, *24*(3), 303–314.

Reagh, Z. M., & Yassa, M. A. (2014). Object and spatial mnemonic interference differentially engage lateral and medial entorhinal cortex in humans. *Proceedings of the National Academy of Sciences of the United States of America*, *111*(40), E4264–E4273.

Reas, E. T., Hagler, D. J., White, N. S., Kuperman, J. M., Bartsch, H., Cross, K., Loi, R. Q., Balachandra, A. R., Meloy, M. J., Wierenga, C. E., Galasko, D., Brewer, J. B., Dale, A. M., & McEvoy, L. K. (2017). Sensitivity of restriction spectrum imaging to memory and neuropathology in Alzheimer's disease. *Alzheimer's Research and Therapy*, *9*(1), 1–12.

Rey, A. (1964). *L'examen clinique en psychologie*. Presses Universitaires de France.

Sabuncu, M. R., Desikan, R. S., Sepulcre, J., Yeo, B. T., Liu, H., Schmansky, N. J., Reuter, M., Weiner, M. W., Buckner, R. L., Sperling, R. A., Fischl, B., & Initiative, A.'s. D. N. (2011). The dynamics of cortical and hippocampal atrophy in Alzheimer disease. *Archives of Neurology*, *68*(8), 1040–1048.

Salo, R. A., Miettinen, T., Laitinen, T., Gröhn, O., & Sierra, A. (2017). Diffusion tensor MRI shows progressive changes in the hippocampus and dentate gyrus after status epilepticus in rat – Histological validation with Fourier-based analysis. *NeuroImage*, *152*, 221–236.

Saritas, E. U., Cunningham, C. H., Lee, J. H., Han, E. T., & Nishimura, D. G. (2008). DWI of the spinal cord with reduced FOV single-shot EPI. *Magnetic Resonance in Medicine*, *60*, 468–473.

Seeger, A., Schulze, M., Schuettauf, F., Ernemann, U., & Hauser, T. K. (2018). Advanced diffusion-weighted imaging in patients with optic

neuritis deficit - value of reduced field of view DWI and readout-segmented DWI. *The Neuroradiology Journal*, 31(2), 126–132.

Sim, K. C., Park, B. J., Han, N. Y., Sung, D. J., Kim, M. J., & Han, Y. E. (2020). Efficacy of ZOOMit coronal diffusion-weighted imaging and MR texture analysis for differentiating between benign and malignant distal bile duct strictures. *Abdominal Radiology (New York)*, 45(8), 2418–2429.

Small, S. A., Chawla, M. K., Buonocore, M., Rapp, P. R., & Barnes, C. A. (2004). Imaging correlates of brain function in monkeys and rats isolates a hippocampal subregion differentially vulnerable to aging. *Proceedings of the National Academy of Sciences*, 101, 7181–7186.

Stark, S. M., Stevenson, R., Wu, C., Rutledge, S., & Stark, C. E. (2015). Stability of age-related deficits in the mnemonic similarity task across task variations. *Behavioral Neuroscience*, 129(3), 257–268.

Stolp, H. B., Ball, G., So, P. W., Tournier, J. D., Jones, M., Thornton, C., & Edwards, A. D. (2018). Voxel-wise comparisons of cellular microstructure and diffusion-MRI in mouse hippocampus using 3D bridging of optically-clear histology with neuroimaging data (3D-BOND). *Scientific Reports*, 8(1), 1–12.

Teipel, S. J., Grothe, M., Lista, S., Toschi, N., Garaci, F. G., & Hampel, H. (2013). Relevance of magnetic resonance imaging for early detection and diagnosis of Alzheimer disease. *The Medical Clinics of North America*, 97, 399–424.

Whittaker, H. T., Zhu, S., Di Curzio, D. L., Buist, R., Li, X. M., Noy, S., Wiseman, F. K., Thiessen, J. D., & Martin, M. (2018). T1, diffusion tensor, and quantitative magnetization transfer imaging of the hippocampus in an Alzheimer's disease mouse model. *Magnetic Resonance Imaging*, 50, 26–37.

Wu, D., & Zhang, J. (2016). In vivo mapping of macroscopic neuronal projections in the mouse hippocampus using high-resolution diffusion MRI. *NeuroImage*, 125, 84–93.

Yassa, M. A., Lacy, J. W., Stark, S. M., Albert, M. S., Gallagher, M., & Stark, C. E. (2011). Pattern separation deficits associated with increased hippocampal CA3 and dentate gyrus activity in nondemented older adults. *Hippocampus*, 21(9), 968–979.

Yassa, M. A., & Stark, C. E. L. (2011). Pattern separation in the hippocampus. *Trends in Neurosciences*, 34(10), 515–525.

Yassa, M. A., Stark, S. M., Bakker, A., Albert, M. S., Gallagher, M., & Stark, C. E. (2010). High-resolution structural and functional MRI of hippocampal CA3 and dentate gyrus in patients with amnestic mild cognitive impairment. *NeuroImage*, 51(3), 1242–1252.

Yeh, F. C., & Ho, C. (2014). Mapping immune cells infiltration using restricted diffusion MRI. *Magnetic Resonance in Medicine*, 77(2), 603–612.

Yushkevich, P. A., Pluta, J., Wang, H., Ding, S. L., Xie, L., Gertje, E., Mancuso, L., Kliot, D., Das, S. R., & Wolk, D. A. (2014). Automated Volumetry and regional thickness analysis of hippocampal subfields and medial temporal cortical structures in mild cognitive impairment. *Human Brain Mapping*, 36, 258–287.

Zarow, C., Vinters, H. V., Ellis, W. G., Weiner, M. W., Mungas, D., White, L., & Chui, H. C. (2005). Correlates of hippocampal neuron number in Alzheimer's disease and ischemic vascular dementia. *Annals of Neurology*, 57(6), 896–903.

Zhang, H., Schneider, T., Wheeler-Kingshott, C. A., & Alexander, D. C. (2012). NODDI: practical in vivo neurite orientation dispersion and density imaging of the human brain. *NeuroImage*, 61(4), 1000–1016.

SUPPORTING INFORMATION

Additional supporting information can be found online in the Supporting Information section at the end of this article.